World Conference on
Timber Engineering
Oslo 2023

SHEAR FAILURE MECHANISM III IN CROSS LAMINATED TIMBER – NUMERICAL INVESTIGATIONS OF FRACTURE BEHAVIOUR

Henrik Danielsson[1], Erik Serrano[2]

ABSTRACT: The paper deals with numerical investigations of load-bearing capacity and fracture behaviour of Cross Laminated Timber at in-plane shear loading. Focus is on shear failure mechanism III, *i.e.* failure in the crossing areas between flatwise bonded laminations, and on evaluating test methods for that failure mode. In current design provisions, this failure mode is characterised by the rolling shear strength, $f_{v,R}$, and the torsional shear strength, $f_{v,tor}$, and therefore testing including both transverse (rolling) shear and torsional shear is needed. Two such test set-ups are investigated, one aiming at evaluating torsional shear strength and one aiming at evaluating rolling shear strength. Full 3D finite element analyses applying a cohesive zone model approach were used to study the strength and fracture behaviour. Failure criteria for structural design, material strength parameters, and the suitability of the two test configurations to determine strength parameters are discussed in relation to findings from the numerical investigations. One main conclusion from the investigation is that expected test results using the torsional test set-up are less size dependent as compared to test results using the transverse set-up. The numerical analyses suggest a very small influence from tensile loading perpendicular to the crossing area, for both test set-ups.

KEYWORDS: CLT, in-plane shear, failure mechanism III, fracture mechanics, finite element modelling

1 INTRODUCTION

Prediction of load-bearing capacity of Cross Laminated Timber (CLT) at in-plane shear loading (see Figure 1) is relatively complex and involves three potential shear failure mechanisms (FM): Gross shear failure (I), net shear failure and (II) and shear failure at the crossing areas between bonded laminations of adjacent layers (III).

This paper deals with investigations regarding load-bearing capacity and fracture behaviour for shear FM III, based on 3D finite element (FE) models including a cohesive zone modelling approach to describe the fracture behaviour at the crossing area between flatwise bonded laminations. The numerical studies include test configurations for determination of strength parameters to be used for structural design: one test set-up for torsional shear loading and one for uniaxial shear force loading.

The influence of test specimen geometry, test specimen size and lamination growth ring pattern on the fracture over the crossing area and on the load-bearing capacity is studied.

The purpose of the work presented is to gain knowledge of the fracture behaviour of CLT at in-plane shear loading, specifically for combined rolling and longitudinal shear over the crossing areas.
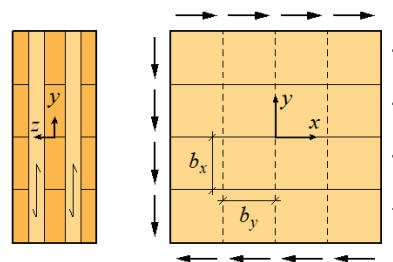

Figure 1: *CLT at in-plane shear loading*

For the applied cohesive zone modelling approach, the behaviour is governed by the material strength, the stiffness, the fracture energy, and the shape of the curve

[1] Henrik Danielsson, Division of Structural Mechanics, Lund University, P.O. Box 118, SE-221 00 Lund, Sweden. Email: henrik.danielsson@construction.lth.se
[2] Erik Serrano, Division of Structural Mechanics, Lund University, P.O. Box 118, SE-221 00 Lund, Sweden.

describing the stress versus deformation relationship within the fracture process region. For rolling shear, very little information is found in the research literature regarding fracture properties at the local scale. For the present application, with combined longitudinal and rolling shear loading, the lack of available information is even further emphasized.

2 FAILURE CRITERIA FOR DESIGN

FM III is in general relevant for CLT elements without edge-bonding, involving shear stresses acting in the *xy*-plane (see Figure 1) and over the crossing areas between adjacent laminations of different layers. These shear stresses represent both longitudinal shear and rolling shear in the two bonded laminations.

For structural design of CLT, both *pure in-plane shear* loading and in-plane shear loading at *beam loading conditions* is relevant. The following failure criteria have been proposed in [1, 2] to be used for structural design:

$$\frac{\tau_{\text{tor}}}{f_{\text{v,tor}}} + \frac{\tau_{zx}}{f_{\text{v,R}}} \leq 1.0 \quad \text{and} \quad \frac{\tau_{\text{tor}}}{f_{\text{v,tor}}} + \frac{\tau_{zy}}{f_{\text{v,R}}} \leq 1.0 \qquad (1a, 1b)$$

Here τ_{tor} is a shear stress due to torsion by relative rotation between the laminations and τ_{zx} and τ_{zy} are the shear stresses due to relative translation between the laminations (see Figure 2). The corresponding strength parameters are the rolling shear strength, $f_{\text{v,R}}$, and a torsional shear strength parameter, $f_{\text{v,tor}}$.

In structural design, the two shear stress components τ_{zx} and τ_{zy} are commonly assumed to have uniform distributions over the crossing areas. The torsional stress τ_{tor} is calculated from the polar moment of inertia, $I_{\text{P,CA}}$, of the bonded area according to

$$\tau_{\text{tor}} = \frac{M_{\text{tor}}}{I_{\text{P,CA}}} \frac{b_{\max}}{2} \quad \text{with} \quad I_{\text{P,CA}} = \frac{b_x b_y}{12}\left(b_x^2 + b_y^2\right) \qquad (2)$$

where M_{tor} is the torsional moment, b_x and b_y are the widths of the laminations, and where $b_{\max} = \max\{b_x, b_y\}$. The stress τ_{tor} according to Equation (2) refers to the maximum value at the four mid-points of the sides of the crossing area, see Figure 2, and can also be expressed as

$$\tau_{\text{tor}} = \frac{M_{\text{tor}}}{W_{\text{P,CA}}} \quad \text{with} \quad W_{\text{P,CA}} = \frac{b_x b_y}{6 b_{\max}}\left(b_x^2 + b_y^2\right) \qquad (3)$$

where $W_{\text{P,CA}}$ represents a corresponding torsional section modulus.

As pointed out in [3], it is from the view of continuum mechanics confusing that the shear stress components in Equations (1a) and (1b) are evaluated against two different strength values: $f_{\text{v,R}}$ for stress components τ_{zx} and τ_{zy}, and $f_{\text{v,tor}}$ for the torsional shear stress τ_{tor}. The torsional shear strength should in this this sense be seen as representing a structural property, rather than a material property.
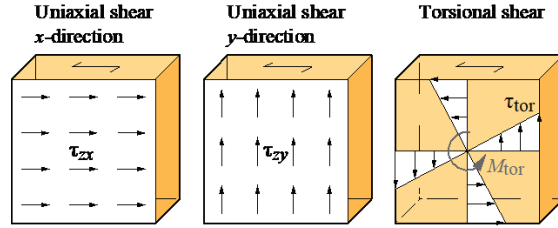

Figure 2: Illustrations of assumed shear stress distributions

Alternative approaches for verification of the load-bearing capacity for shear FM III are outlined in [3] and further discussed in [4]. This approach is based on consideration of only the rolling shear strength of the laminations, which would make it possible to abandon the torsional shear strength parameter, $f_{\text{v,tor}}$. This is motivated by the relatively large difference in material strength between rolling shear and longitudinal shear. For orthogonally bonded laminations, a material point on one side of the bonding area loaded in longitudinal shear will have a neighbouring material point on the other side of the bonding area which is loaded in rolling shear. By this reasoning, a *maximum stress* criterion based on the rolling shear strength of the lamination was suggested in [3], according to the illustration in Figure 3 (which is based on an assumed strength ratio as $f_{\text{v}}/f_{\text{v,R}} = 2.0$).
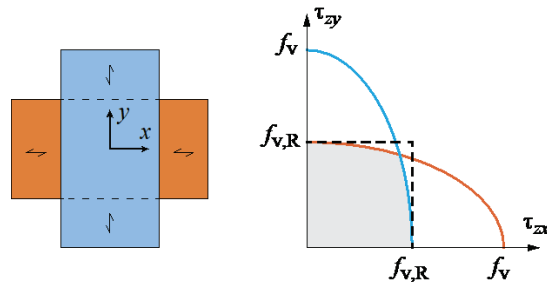

Figure 3: Suggested maximum stress criterion from [3], based on only rolling shear strength $f_{\text{v,R}}$ (dashed lines)

3 ANALYTICAL MODELS

Simple analytical models can be formulated for approximate estimation of the load-bearing capacity of a crossing area loaded in either pure uniaxial shear or in torsion. A system of two rigid surfaces, connected by a shear-flexible medium, is considered. Two different failure/yield surfaces are considered here. These are denoted A and B and are based on a quadratic stress interaction and on a maximum stress criterion, according to Equations (4) and (5), respectively. The yield surfaces are illustrated in Figure 4, with f_{s} representing the shear strength.

Surface A: $\qquad \sqrt{\tau_{zx}^2 + \tau_{zy}^2} \leq f_{\text{s}}$ $\qquad (4)$

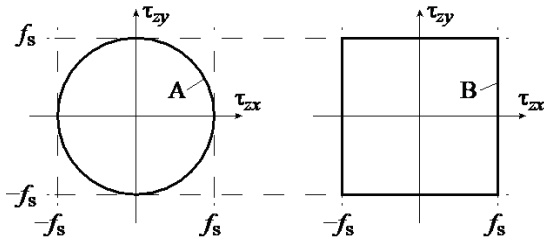Surface B: $\qquad \max\{\tau_{zx}, \tau_{zy}\} \leq f_{\text{s}}$ $\qquad (5)$

Figure 4: Failure/yield surfaces A and B

Expressions for the elastic and ideally plastic load-bearing capacities for a square area loaded in uniaxial shear or in torsion are given in [4] for the respective failure/yield surfaces. These elastic/plastic limits are used below, for comparison to results obtained by numerical analyses.

4 NUMERICAL MODELLING

Test configurations for determination of the rolling shear strength, $f_{v,R}$, and the torsional shear strength parameter, $f_{v,tor}$, were studied by numerical methods. The numerical models are based on non-linear FE-modelling and a cohesive zone approach, including strain softening after reaching the local material strength, for modelling of the fracture initiation and propagation over the crossing area.

The studied test configurations include situations of torsional loading and uniaxial shear force loading. For these test configurations, numerical parameter studies were carried out in order to investigate the influence of specimen geometry (lamination sizes) and the influence of the growth ring pattern of the laminations on the load-bearing capacity and fracture behaviour.

The software Abaqus [5, 6] was used for the numerical analyses. The timber laminations were modelled as linear elastic parts with orthotropic stiffness properties according to Table 1 and considering a cylindrical coordinate system, LRT. Linear 3D brick elements (C3D8 in Abaqus) were used for the timber laminations. The bonding between the laminations was modelled as a surface-to-surface contact. The contact formulation was assigned as hard contact in compression normal to the contact surface. For the two in-plane shear directions and for the normal direction in tension, a cohesive behaviour was implemented. This behaviour is defined by local material strengths for the two in-plane shear directions (f_{s1} and f_{s2}), the tensile strength for loading perpendicular to the contact surface (f_n), the fracture energy (G_f) and a softening law defining the descending part of the local stress versus deformation response. The initial stiffness for the contact formulation in the two shear directions and in the normal direction is further defined by the stiffness values k_{s1}, k_{s2} and k_n, respectively.

For the parameters defining the contact formulation and the softening behaviour, reference values were chosen in accordance with the reference values used in [4]: $f_{s,1} = f_{s,2} = 3.0$ MPa, $f_n = 5.0$ MPa, $G_f = 1.2$ Nmm/mm² and $k_{s1} = k_{s2} = k_n = 100$ N/mm³. For the softening, a linear relation between deformation and decreasing stress was assumed.

Table 1: Material stiffness parameters used for the timber laminations

Modulus of Elasticity	E_L	12 000	MPa
	E_T	400	MPa
	E_R	600	MPa
Shear modulus	G_{LT}	750	MPa
	G_{LR}	600	MPa
	G_{TR}	75	MPa
Poisson's ratio	ν_{LT}	0.50	-
	ν_{LR}	0.50	-
	ν_{TR}	0.33	-

In order to study the influence of the choice of damage initiation criterion, two different criteria were used. A maximum stress criterion according to

$$\max\left\{\frac{\langle\sigma_n\rangle}{f_n},\frac{\tau_{s1}}{f_{s1}},\frac{\tau_{s2}}{f_{s2}}\right\} = 1.0 \tag{6}$$

and a criterion considering quadratic stress interaction according to

$$\left(\frac{\langle\sigma_n\rangle}{f_n}\right)^2 + \left(\frac{\tau_{s1}}{f_{s1}}\right)^2 + \left(\frac{\tau_{s2}}{f_{s2}}\right)^2 = 1.0 \tag{7}$$

were considered. For these criteria, σ_n represents the normal (tensile) stress over the crossing area while τ_{s1} and τ_{s2} represent the two in-plane shear stresses. For all analyses presented below, equal values for the two in-plane shear strengths are assumed and a notation as $f_{s1} = f_{s2} = f_s$ is hence used below.

For comparison of results, a non-dimensional brittleness ratio is defined according to b/l_{ch}, where b is a characteristic length of the considered body and where the material characteristic length is defined according to

$$l_{ch} = \frac{G_{TR}G_f}{f_s^2} \tag{8}$$

where G_{TR} is the rolling shear stiffness, G_f the fracture energy and f_s the local material shear strength. With reference values for these parameters as given above, the characteristic material length is $l_{ch} = 10$ mm.

4.1 TORSIONAL SHEAR LOADING

For pure torsional loading, the test set-up suggested in EN 16351:2021 [7] (as an alternative method) for determination of the torsional shear strength parameter $f_{v,tor}$ is considered.

The specimen geometry is shown in Figure 5, while the applied boundary conditions and considered lamination growth ring patterns are illustrated in Figures 6 and 7, respectively. For the back surface of the lamination with grain direction parallel to the x-direction, displacements were prescribed as $u_x = u_y = u_z = 0$. The front surface of the lamination with grain direction parallel to the y-direction, was constrained by a kinematic coupling to the surface midpoint which was used as a reference point. For this reference point, boundary conditions were implemented such that the displacements $u_x = u_y = u_z = 0$ and the loading was applied by a prescribed rotation θ_z.
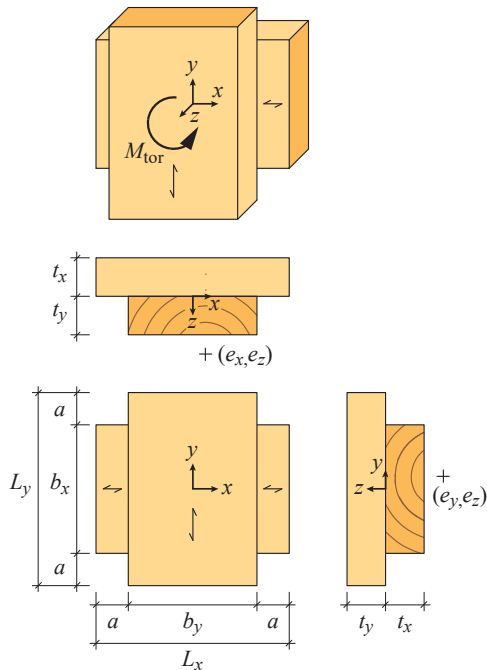
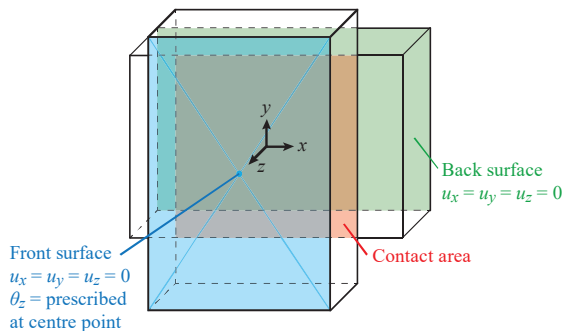**Figure 5:** *Definition of geometry for pure torsional loading*

Figure 6: *Boundary conditions for pure torsional loading*

According to EN 16351:2021, no restraints from compression or tension in the direction of the rotation axis should be introduced. The influence of boundary conditions was studied by releasing the constraint of the displacement in the z-direction for the front surface, *cf.* Figure 6.

The lamination lengths (here denoted L_x and L_y) should according to EN 16351:2021 furthermore be such that the laminations extend a minimum of 30 mm on each side of the tested crossing area. No further instructions are given regarding the absolute or relative size of the laminations.

Torsional tests of single crossing areas are reported in [8, 9], for six test series with different lamination growth ring patterns and crossing area sizes: 145×100 mm², 145×150 mm² and 145×200 mm². Those tests gave an overall mean torsional strength of 3.46 MPa, with test series mean values varying between 3.00 MPa and 4.13 MPa, without a clear trend regarding the size influence on the load-bearing capacity.

Numerical results for models loaded in pure torsional shear are expressed by the *apparent* torsional shear stress as defined according to Equations (2) and (3), using the resulting torsional moment over the crossing area M_{tor} as found from the FE-analyses.

An initial parameter study was carried out, aimed at investigating the influence of model parameters on the numerical results. Based on the reference values of material strengths, fracture energy and lamination stiffness properties as defined above, a parameter study on the influence of the initial stiffness of the contact area was performed. Stiffness values $k_{s1} = k_{s2} = k_n$ in the range from 10 N/mm³ to 4 000 N/mm³ were used. The lamination geometry was defined by setting $b = b_x = b_y = 120$ mm, $t_x = t_y = 30$ mm and $a = 30$ mm, and the growth ring pattern RB was considered. The element mesh was chosen to obtain roughly cubically shaped elements with a side length of approximately $t_x/6 = 5$ mm.

The calculated maximum load increases slightly with increased crossing area stiffness. The reference stiffness (100 N/mm³) gives however only a 0.7% difference in maximum value compared to a stiffness of 4 000 N/mm³. Since the numerical stability is enhanced using moderate crossing area stiffness values, the reference stiffness of 100 N/mm³ was considered as a reasonable trade-off between numerical stability and accuracy.

The influence of the element size on the results was also studied. Decreasing the element side length by a factor 2.0 (from 5 mm to 2.5 mm) gave only a 0.2% difference in maximum load. The difference in overall torsional stiffness of the specimen was influenced to a greater extent by that element refinement: a reduction of the stiffness by 1.5% was found. An approximate element side length of 1/6 of the lamination width was used for results presented below and relating to torsional loading, since it was considered as a reasonable trade-off between numerical efficiency and accuracy.
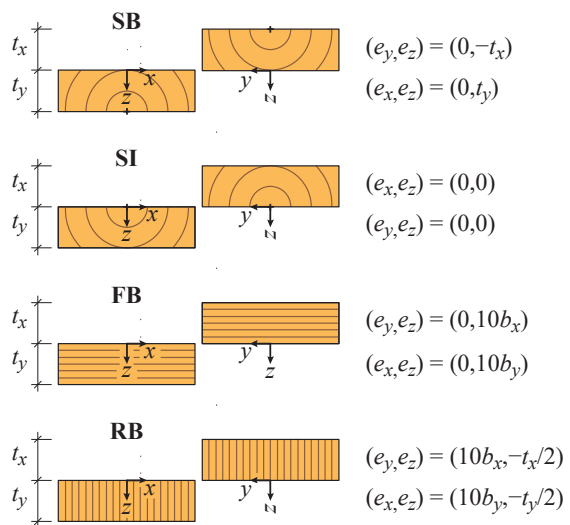

Figure 7: *Considered growth ring patterns for pure torsional loading*

Results for analyses considering the two different criteria for damage initiation according to Equations (6) and (7) are shown in Figure 8. For both criteria, results are presented for assumptions of material tensile strength as either f_n = 5.0 MPa (reference value) or f_n = 2.5 MPa and for boundary conditions as prescribed by EN 16351:2021, *i.e.* with $u_x = u_y = 0$ but disregarding $u_z = 0$ for the surface with prescribed rotation (denoted EN in Figure 8). The results relate to a specimen with geometry $b_x = b_y = 120$ mm, $t_x = t_y = 30$ mm, $a = 30$ mm and with growth ring pattern RB according to Figure 7.

Using the maximum stress criterion (MS) according to Equation (6) compared to the quadratic interaction criterion (QT) according to Equation (7) gives an increase of the maximum apparent torsional stress of about 6%. Within the two groups of curves (three curves in each group), representing the two criteria, very similar or identical results were found. Identical results for the torsional shear stress were found for material tensile strengths f_n = 2.5 MPa, 5.0 MPa and 50 MPa (not shown in Figure 8) for the maximum stress criterion. A very small influence of the material tensile strength was also found for the damage initiation criterion based on quadratic traction (QT), with differences being below 0.2% for load-bearing capacity. The change of boundary conditions regarding free/restricted movement in the z-direction has also a very small influence on the load-bearing capacity, for both damage initiation criteria.

The response in terms of the apparent torsional stress versus prescribed rotation is shown in Figure 9 for $b_x = b_y = 120$ mm, $t_x = t_y = 30$ mm, $a = 30$ mm, growth ring pattern RB, reference values for materials strengths and using the damage initiation criterion based on maximum stress. For these results, a slightly refined mesh was used with approximate elements side lengths as $t_x/8$. In subfigures a), b) and c), the stress distributions over the crossing area are illustrated by the maximum value of the two shear stress components τ_{zx} and τ_{zy} acting in the plane of the crossing area, at three instants during loading: a) at initiation of softening, b) about midway between initiation of softening and maximum load and c) at maximum load.
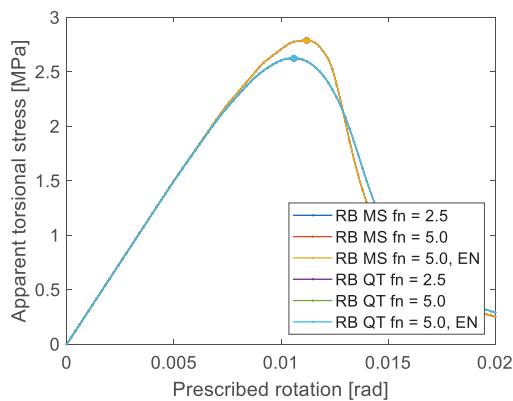

Figure 8: Apparent torsional stress versus prescribed rotation for different choices of criteria for initiation of softening (MS and QT), for different material tensile strengths f_n, and for different boundary conditions
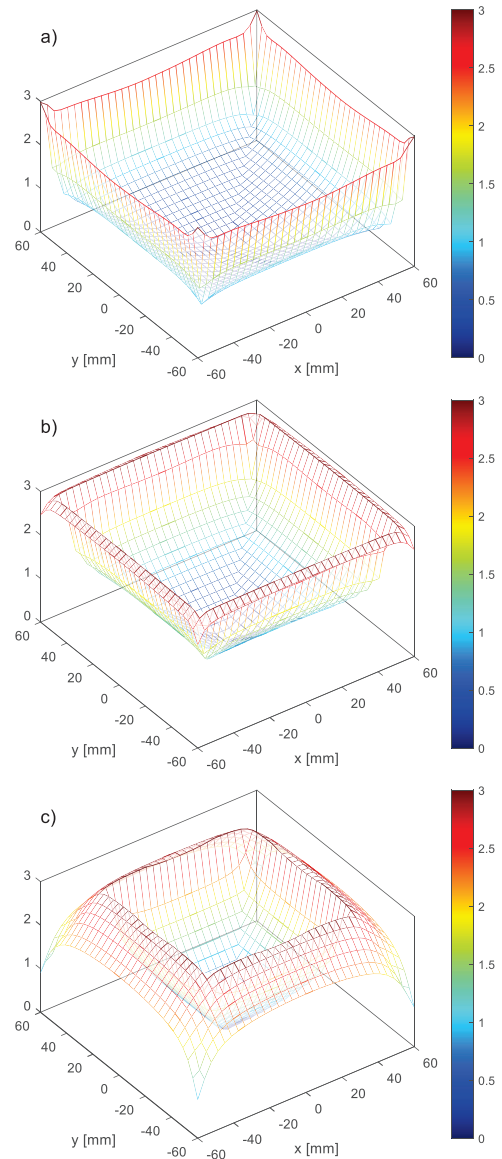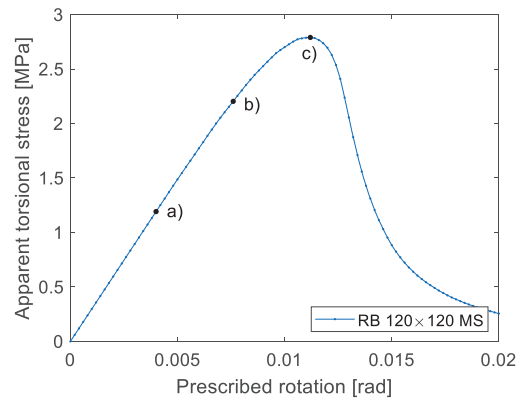

Figure 9: Apparent torsional stress versus rotation for geometry RB 120×120 with damage initiation criterion from Equation (6) and stress distributions for $\tau = max(\tau_{zx}, \tau_{zy})$ at instants a), b) and c) during loading

Results in terms of apparent torsional strength are given in Figure 10, based on a specimen geometry with $b = b_x = b_y$, $L_x = L_y = 1.5b_x$, and $t_x = t_y = b_x/4$ and for lamination widths b within the range of 5 mm to 200 mm. Results for all geometries, and all growth ring patterns as illustrated in Figure 7 and considering the damage initiation criteria according to Equation (6) are given. In addition, results for growth ring pattern RB, and initiation criterion according to Equation (7) are also shown. For the specimen geometries considered here, the demand $a \geq 30$ mm given in EN 16351:2021 is not fulfilled for laminations widths $b < 120$ mm.

The same results are shown in Figure 11, but now expressed as the relationship between the brittleness ratio b/l_{ch} and the normalised torsional strength, $\tau_{tor,max}/f_s$. The considered lamination widths b give brittleness ratios b/l_{ch} in the range of 0.5 to 20.

The differences in load-bearing capacity between the different growth ring patterns is fairly small and there is no strong influence of the specimen size for practically relevant dimensions of the laminations.
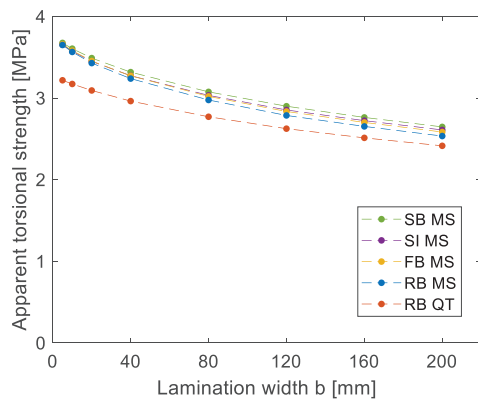

Figure 10: Apparent torsional shear strength, $M_{tor,max}/W_{P,CA}$ according to Equation (3), for different growth ring patterns and lamination widths $b = b_x = b_y$
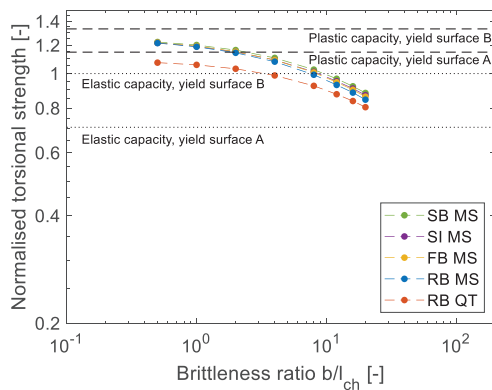

Figure 11: Normalised torsional strength, $\tau_{tor,max}/f_s$, as influenced by brittleness ratio for different growth ring patterns and considering damage initiation criteria according to Equations (6) and (7)

The influence of the individual lamination widths, and hence the size and shape of the crossing area, was studied. Results for different widths b_y (20 mm to 220 mm) of the lamination oriented in the y-direction, for a fixed width $b_x = 120$ mm of the lamination oriented in the x-direction, are shown in Figure 12. These results are based on lamination thicknesses $t_x = t_y = 30$ mm, $a = 30$ mm, growth ring pattern RB according to Figure 7 and damage initiation according to Equation (6).
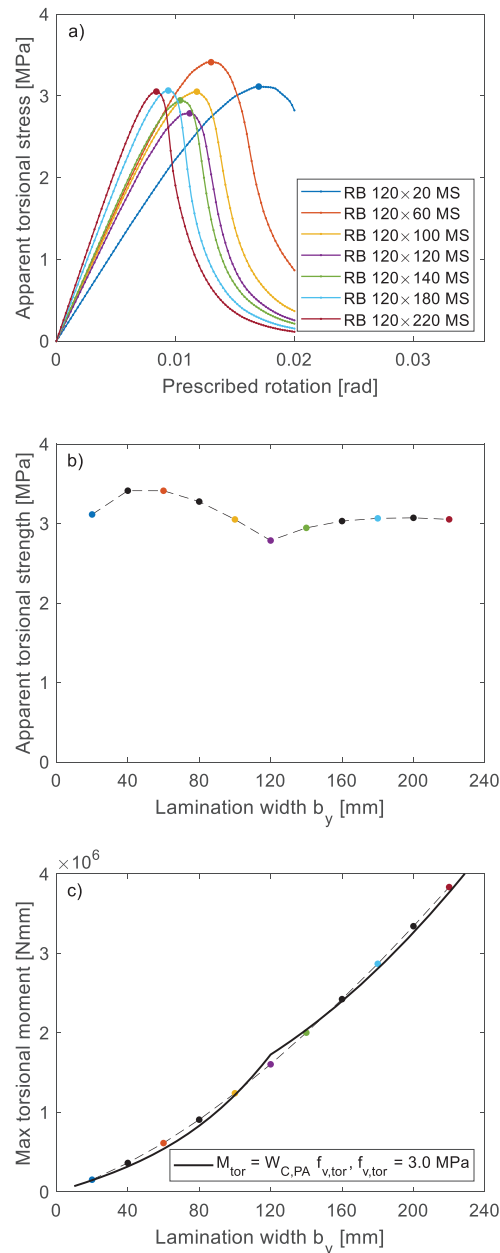

Figure 12: Results for $b_x = 120$ mm and different lamination widths b_y in terms of a) torsional stress versus rotation, b) apparent torsional strength and c) maximum torsional moment

Results presented in Figure 12 relate to specimens with 11 different geometries. Results in terms of apparent torsional stress versus rotation are shown in Figure 12a) for seven of these analyses, while results in Figures 12b) and c) are given for all 11 geometries.

The differences in the apparent torsional strength according to Figure 12b) can be explained by essentially two effects; a size effect and an effect of the change of the specimen shape. The two geometries with laminations $b_x \times b_y = 120 \times 80$ mm^2 and $b_x \times b_y = 120 \times 180$ mm^2 are equal in shape with a ratio of 1:1.5 between the side lengths of the crossing area. The difference in apparent torsional strength, 3.28 MPa for 120×80 mm^2 and 3.07 MPa for 120×180 mm^2, is hence related to a size effect and, possibly to the effect of changed stiffness ratio between the crossing area torsional stiffness and the rolling shear stiffness of the laminations.

The maximum torsional moments are shown in Figure 12c), where also the torsional moment capacity according to the design criteria from Equations (1) – (3) is given for an assumed torsional strength parameter $f_{v,tor} = 3.0$ MPa. The ratio between the numerically found values of the maximum torsional moment and the capacity according to the design criteria varies between 0.93 and 1.14 for this assumption.

In order to further study the influence of the shape of the crossing area, a number of analyses were carried out for geometries with a fixed value of the torsional section modulus defined in Equation (3), $W_{P,CA} = 576\ 000$ mm^3 (as for $b_x = b_y = 120$ mm), by varying both lamination widths, b_x and b_y. Also for these analyses, geometries with lamination thicknesses $t_x = t_y = 30$ mm and $a = 30$ mm were considered and results are presented in Figure 13.

Results in terms of stress versus rotation response are given in Figure 13a) for six out of the 11 geometries considered. The apparent torsional strength is shown in Figure 13b) and the maximum torsional moment in Figure 13c).

From the present results, a maximum load-bearing capacity appears to be found for a side length ratio of the crossing area of about 1.8. Equal lamination widths (here $b_x = b_y = 120$ mm) and hence a square shape of the crossing area gives the lowest load-bearing capacity among the geometries considered here. The difference between the highest and lowest capacities (found for geometries 174×90 mm^2 and 120×120 mm^2, respectively) is 15%.

The maximum torsional moments are shown in Figure 13c), where also the torsional moment capacity according to the design criteria from Equation (1) – (3) is given for an assumed value $f_{v,tor} = 3.0$ MPa. The ratio between the numerically found values of maximum torsional moment and the design criteria varies between 0.93 and 1.07.

The results presented in Figures 12 and 13 concern specimen geometries with a large span of the aspect ratio of the crossing area side lengths: ratios up to 1:6 for results presented in Figure 12 and ratios up to 1:3 for results

presented in Figure 13. The numerical results in terms of the maximum torsional moment are yet in fairly good agreement with the load-bearing capacities given by the design criteria from Equations (1) – (3), with the torsional moment capacity being proportional to the value of $W_{P,CA}$, defined in Equation (3).

The shear stress distribution over the crossing area (as found from the FE-analyses) varies during loading, as illustrated in Figure 9, due to initiation of local softening and development of fracture process zones. Although the stress distribution at maximum load does not agree very well with the assumed stress distribution according to the design approach (see Figure 2), similar load-bearing capacities are predicted.
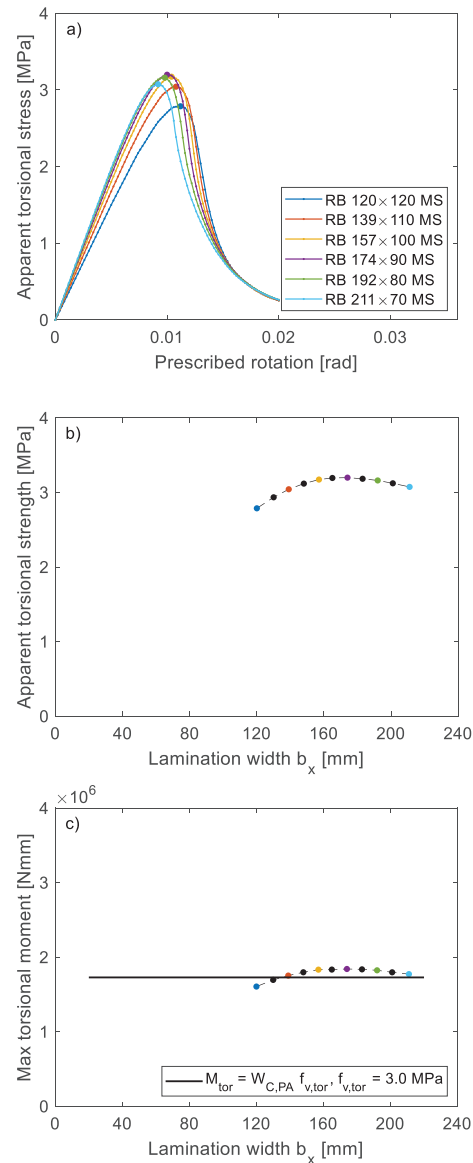

Figure 13: *Results for different laminations widths $b_x \times b_y$ with constant value of $W_{P,CA} = 576\ 000$ mm^3 in terms of a) torsional stress versus rotation, b) apparent torsional strength and c) maximum torsional moment*

4.2 UNIAXIAL SHEAR LOADING

For the load case of *pure uniaxial* shear, a test set-up introducing shear over two crossing areas (by compression loading) of a symmetrical test specimen is considered, as illustrated in Figure 14.

Such tests are for example reported in [10], with specimens cut from CLT with lay-up 40-20-40 and testing a crossing area of 150×150 mm². Tests of six nominally equal samples gave a mean rolling shear strength $f_{v,R} = 1.39$ MPa with CoV = 13%.

The numerical results presented here relate to the influence of specimen size and the influence of the growth ring pattern of the laminations, considering material stiffness properties according to Table 1 and boundary conditions according to Figure 15. For the FE-model, the symmetry with respect to the *z*-direction was considered and only half of the specimen was modelled. The parameters describing the contact formulation and the softening behaviour were according to the reference values stated in Section 4. A study of the influence of the choice for the tensile material strength f_n was carried out and results showed a very small influence on the load bearing capacity for strength values of 2.5 MPa and 50 MPa, compared to the reference value of 5.0 MPa.

For the study of the influence of the specimen size, geometry parameters were chosen according to: $b_x = b_y$, $t_x = t_y = b_x/4$, $L_x = b_x$ and $a = b_x/6$. For this basic geometry, the lamination widths $b = b_x = b_y$ were varied from 5 mm to 200 mm. Three different growth ring orientations were considered for this loading situation, see Figure 16.
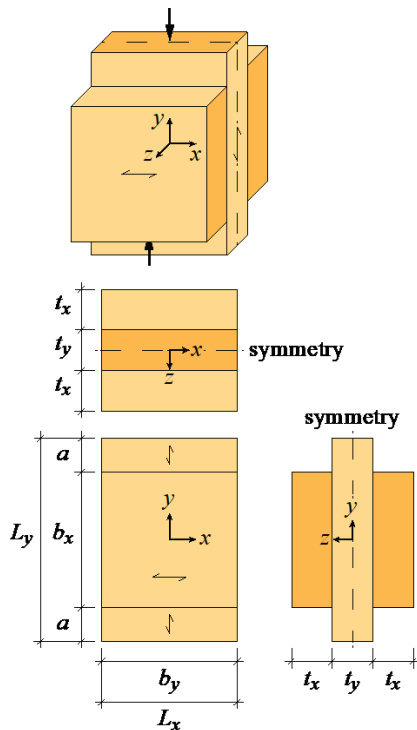

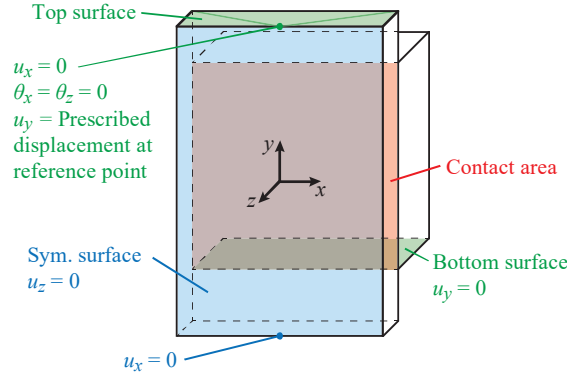*Figure 14: Definition of geometry for pure shear loading*

Figure 15: Boundary conditions for pure shear loading
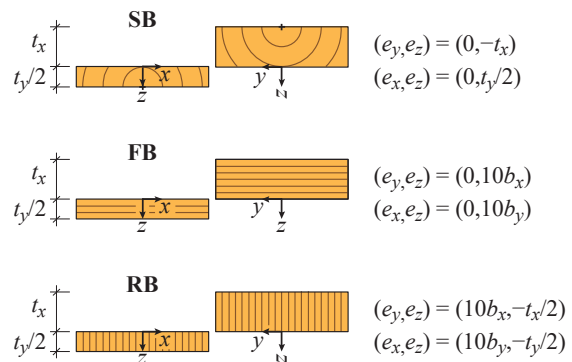

Figure 16: Considered growth ring patterns for pure shear loading

Results in terms of *apparent* shear strength, defined as the mean shear stress over the crossing area at maximum loading, are given in Figure 17. The same results are shown in Figure 18, as the relationship between the brittleness ratio b/l_{ch} and the normalised shear strength.

For growth ring pattern RB, results are presented for damage initiation criteria according to Equations (6) and (7). The differences are overall very small, indicating a uniaxial shear stress distribution over the crossing area with little influence from τ_{zx} on the results.

As the specimen size is decreased, the mean shear stress at maximum load approaches the material strength f_s. For a small size of the crossing area, the fracture process zone is relatively large and the behaviour approaches the case of an ideally plastic behaviour over the crossing area. For a uniform stress distribution, the elastic/plastic capacities for yield/failure surfaces A and B are all equal (f_s).

The numerical results show a strong influence of the specimen size for lamination widths $b = b_x = b_y$ above approximately 100 mm. For these specimen sizes, the trend of the numerical results resembles the size influence predicted by LEFM (the dashed line in Figure 18), with load-bearing capacity inversely proportional to the square root of the size. The size influence found from the numerical analyses presented in Figure 18, considering pure uniaxial shear, is stronger than found for the case of torsional loading with results presented in Figure 11.
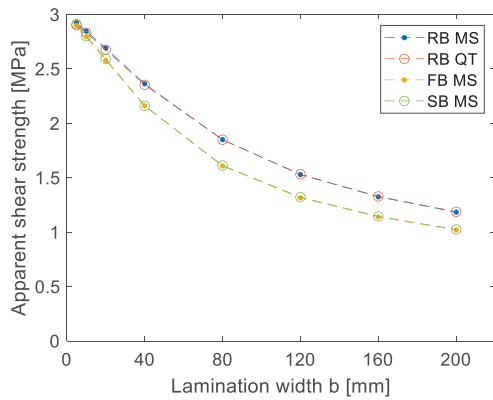
Figure 17: Apparent shear strengths for different growth ring patterns and lamination widths $b = b_x = b_y$ and considering damage initiation criteria according to Equations (6) and (7)
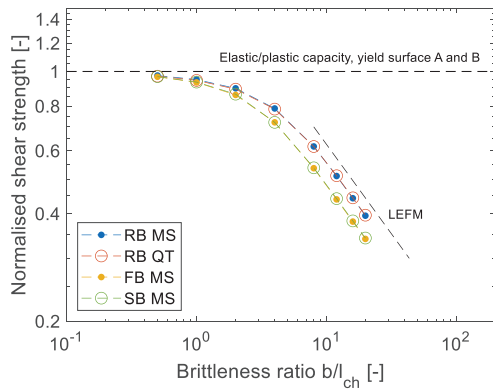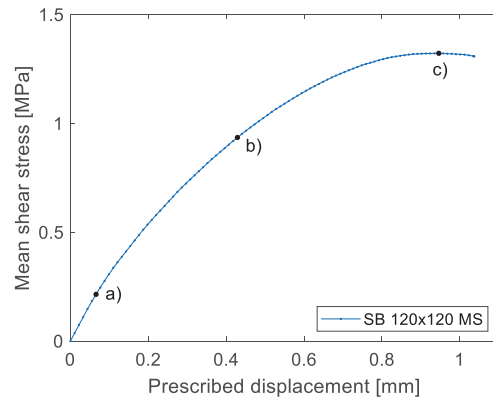

Figure 18: Normalised shear strength as influenced by brittleness ratio for different growth ring patterns and considering damage initiation criteria according to Equations (6) and (7)

The response in terms of mean shear stress versus prescribed displacement is shown in Figure 19, for a specimen with geometry according to $b_x = b_y = 120$ mm, $t_x = t_y = 30$ mm, $a = 20$ mm and with growth ring pattern SB according to Figure 16. The stress distribution for the shear stress component τ_{zy} over the crossing area is illustrated for three instants during loading: a) at initiation of softening, b) about midway between initiation of softening and maximum load and c) at maximum load.

The stress distribution before initiation of softening is very uneven, with a high stress concentration along the edge of the crossing area close to the support. At increased loading, a fracture process zone develops and its front moves in the y-direction at increasing load. At maximum load, a small traction-free crack has formed and the stress at the opposite side of the crossing area is approaching the material strength.

During the complete course of loading, the distribution of the shear stress τ_{zy} is very uniform with respect to the x-direction.
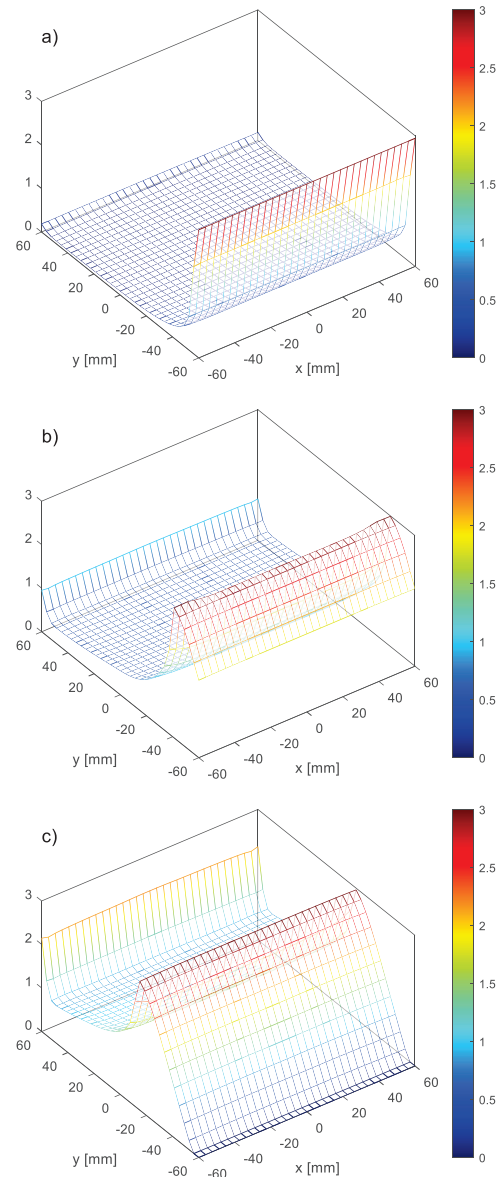

Figure 19: Load versus displacement for geometry SB 120×120 with damage initiation criterion from Equation (6) and stress distributions for τ_{zy} at instants a), b) and c) during loading

5 DISCUSSION AND CONCLUSIONS

The general failure criteria for shear failure mechanism III according to Equations (1a) and (1b) are appealing in the sense that they represent criteria which are easy to use for structural engineers. The concept of using two different strength parameters, the rolling shear strength $f_{v,R}$ and the torsional shear strength $f_{v,tor}$, is however somewhat confusing from the view point of continuum mechanics.

Numerical results for pure torsional loading, based on a cohesive zone modelling approach and use of a damage initiation criterion based on maximum stress values and a single shear strength parameter, f_s, are presented in Figures 12 and 13 for different crossing area sizes and shapes. The numerical analyses gave maximum torsional moments which agree reasonably well with predictions of the design approach according to Equations (1) – (3). This agreement regarding load-bearing capacity is not obvious, since the basic concepts of the numerical modelling approach and of the mechanical model underlying the design approach are very different.

Selecting appropriate values for material parameters (especially material strengths and fracture energy) for the present type of numerical analyses is furthermore not obvious, this issue is discussed in *e.g.* [4]. For the reference values of material parameters used in this work, load-bearing capacities as found for the numerical analyses for both torsional and uniaxial shear loading do however roughly agree with test results as presented in *e.g.* [8–10].

The investigations presented here are limited to consideration of one single crossing area which is loaded in *either* pure torsion *or* uniaxial shear. For practical design situations involving in-plane shear of CLT, such as in-plane beam loading, there is typically a large number of crossing areas within the member with combined torsion and uniaxial shear loading. Proposed design approaches for CLT beams, as presented in [1–2, 11], are based on models considering linear elastic behaviour and do not account for gradual damage and strain-softening over the crossing areas during increased loading. To gain better understanding of the mechanical behaviour, further numerical analyses considering full-sized CLT beams modelled with softening contact are suggested.

Considering the specific test set-ups studied here, one important conclusion is that the set-up for uniaxial shear loading according to Figure 14 should be expected to give results for the rolling shear strength which are highly dependent on the specimen size (see Figure 18), especially for practically relevant lamination dimensions with $b > 100$ mm. The numerical results for the test set-up for torsional loading according to Figure 5 do not show the same strong size influence on the load-bearing capacity (see Figure 11). A drawback of torsional testing may however be that the tests are rather complicated to carry out and that torsional testing machines might not be considered as standard test equipment. From the numerical investigation presented, neither of the test set-ups appear to be influenced by tensile loading perpendicular to the crossing area.

REFERENCES

[1] M. Flaig: Biegeträger aus Brettsperrholz bei Beanspruch in Plattebene. Doctoral thesis. Karlsruhe Institute of Technology, Karlsruhe, Germany, 2013.

[2] M. Flaig, H.J. Blass: Shear strength and shear stiffness of CLT-beams loaded in plane. In: Proc. CIB-W18, CIB-W18/46-12-3, Vancouver, Canada, 2013.

[3] E. Serrano: Test methods for in-plane shear tests of cross laminated timber. In: Properties, testing and design of cross laminated timber: A state-of-the-art report by COST Action FP1402/WG2, Shaker Verlag, Aachen, Germany, 2018.

[4] H. Danielsson, E. Serrano: Cross laminated timber at in-plane shear loading – Strength and fracture analysis of shear mode III. In: Proc. WCTE 2020/21.

[5] Dassault Systemes Simulia Corp. ABAQUS/CAE, Version 2019, 2018.

[6] Dassault Systemes Simulia Corp. ABAQUS/CAE, Version 2021, 2020.

[7] CEN European Committee for Standardization. EN 16351:2021. Timber structures – Cross laminated timber – Requirements.

[8] G. Jeitler: Versuchstechnische Ermittlung der Verdrehungskenngrössen von orthogonal verklebten Brettlamellen. Diploma thesis, TU Graz, 2004.

[9] R. Joebstl, T. Bogensperger et al: Mechanical behaviour of two orthogonally glued boards. In: Proc WCTE, Lahti, Finland, 2004.

[10] M. Jeleč et al: Advancement in prediction of shear strength and stiffness of cross laminated timber beams. *Eng Struct* 238 (2021) 112247.

[11] H. Danielsson, M. Jelec: A unified design proposal for shear stress prediction in crossing areas for cross laminated timber at in-plane shear and beam loading conditions. *Constr Build Mater* 355 (2022) 129167.

https://doi.org/10.52202/069179-0317